NuSTAR tests of sterile-neutrino dark matter: New Galactic bulge observations and combined impact

Brandon M. Roach®, ^{1,*} Kenny C. Y. Ng®, ^{2,†} Kerstin Perez®, ^{1,‡} John F. Beacom®, ^{3,4,5,§} Shunsaku Horiuchi®, ^{6,||} Roman Krivonos®, ^{7,¶} and Daniel R. Wik®^{8,**}

¹Department of Physics, Massachusetts Institute of Technology, Cambridge, Massachusetts 02139, USA ²Department of Particle Physics and Astrophysics, Weizmann Institute of Science, Rehovot 76100, Israel ³Center for Cosmology and AstroParticle Physics (CCAPP), Ohio State University, Columbus, OH 43210, USA

Department of Physics, Ohio State University, Columbus, Ohio 43210, USA
 Department of Astronomy, Ohio State University, Columbus, Ohio 43210, USA
 Center for Neutrino Physics, Department of Physics, Virginia Tech, Blacksburg, Virginia 24061, USA
 Space Research Institute of the Russian Academy of Sciences (IKI), Moscow 117997, Russia
 Department of Physics and Astronomy, University of Utah, Salt Lake City, Utah 84112, USA

(Received 4 October 2019; accepted 2 April 2020; published 8 May 2020)

We analyze two dedicated NuSTAR observations with exposure \sim 190 ks located \sim 10° from the Galactic plane, one above and the other below, to search for x-ray lines from the radiative decay of sterile-neutrino dark matter. These fields were chosen to minimize astrophysical x-ray backgrounds while remaining near the densest region of the dark matter halo. We find no evidence of anomalous x-ray lines in the energy range 5–20 keV, corresponding to sterile neutrino masses 10–40 keV. Interpreted in the context of sterile neutrinos produced via neutrino mixing, these observations provide the leading constraints in the mass range 10–12 keV, improving upon previous constraints in this range by a factor \sim 2. We also compare our results to Monte Carlo simulations, showing that the fluctuations in our derived limit are not dominated by systematic effects. An updated model of the instrumental background, which is currently under development, will improve NuSTAR's sensitivity to anomalous x-ray lines, particularly for energies 3–5 keV.

DOI: 10.1103/PhysRevD.101.103011

I. INTRODUCTION

Multiple lines of cosmological evidence indicate that $\sim 80\%$ of the matter density of the Universe, and $\sim 25\%$ of its energy density, is nonbaryonic and nonluminous, hence its name, dark matter (DM) [1]. At present, the effects of DM are only measurable via its gravitational effects on astronomical scales, ranging from the motions of galaxies and galaxy clusters to the power spectrum of the cosmic microwave background [2–7]. The lack of a viable Standard Model candidate for particle DM (hereafter symbolized χ) has led to a plethora of theoretical models, many of which are also motivated by a desire to account for other phenomena not explained by the Standard

Model (e.g., baryogenesis, neutrino masses, the hierarchy problem, etc).

The techniques of indirect detection use astronomical observations to search for the decay and/or annihilation of DM into Standard Model particles such as electrons/positrons, (anti)protons/nuclei, neutrinos, and photons [8]. Because photons are not deflected by astrophysical magnetic fields, it is possible to determine their arrival direction within the angular resolution of the detector, allowing for a rejection of photons from known astrophysical sources. Final states with monoenergetic photons are particularly valuable for indirect DM searches, as they result in linelike signals atop a (usually) smooth continuum background.

A popular DM candidate with $m_{\chi} \sim \text{keV}$ is the sterile neutrino, with models such as the νMSM providing explanations for the particle nature of DM, neutrino masses, and baryogenesis [9–12]. The radiative decay of sterile neutrinos via $\chi \to \nu + \gamma$ would produce a monoenergetic x-ray photon and an active neutrino, each with $E = m_{\chi}/2$ [13–20].

Sterile neutrinos may be produced in the early Universe via mixing with active neutrinos [21], and this production

roachb@mit.edu

chun-yu.ng@weizmann.ac.il

^{*}kmperez@mit.edu

beacom.7@osu.edu

horiuchi@vt.edu

krivonos@iki.rssi.ru

^{*}wik@astro.utah.edu

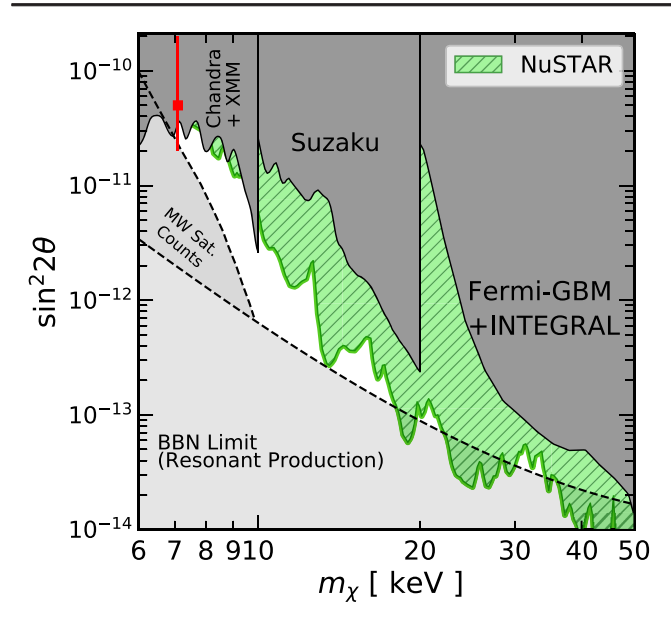


FIG. 1. The combined impact on the ν MSM parameter space of previous NuSTAR searches [30–33] and this work is indicated by the green region. This work provides the leading constraints in the 10–12 keV mass range, as shown in Fig. 5. The tentative $E \simeq 3.5$ keV signal [34–36] is indicated by the red point. Constraints from other x-ray instruments [37–41] are shown for comparison. Uncertainties associated with MW satellite counts [28] and BBN [26,27] are discussed in Sec. I.

may be resonantly enhanced by primordial lepton asymmetry [22]. Considerations from big bang nucleosynthesis (BBN) [23-25] provide an upper bound on the cosmological lepton asymmetry per unit entropy density $L_6 \equiv 10^6 (n_{\nu} - n_{\bar{\nu}})/s \le 2500$, which we translate into the constraint on the active-sterile mixing angle $\sin^2 2\theta$ shown in Fig. 1 using the STERILE-DM code [26]. We note that these BBN limits are particularly sensitive to the treatment of neutrino opacities and the plasma equation of state near the OCD phase transition, with different calculations finding different results-for example, the limits shown in Refs. [25,27] for the same value of L_6 are nearly an order of magnitude less constraining than those from Ref. [26], which the authors of Refs. [16,28] attribute to differences in the treatment of neutrino opacities in the QCD epoch. (An update to the calculation in Ref. [27] is presented in Ref. [29], though the latter does not present an updated constraint in the $m_{\gamma} - \sin^2 2\theta$ plane.) This lower bound may evolve as calculations are refined.

An additional indirect constraint on sterile-neutrino DM arises from comparing the observed number of Milky Way (MW) satellite galaxies to the results of N-body cosmological simulations. Compared to cold DM, warm DM particles are expected to suppress the matter power spectrum at small scales, reducing the number of low-mass DM subhaloes orbiting the Galaxy. In Fig. 1, we adopt the result of Ref. [28] with $N_{\text{subhalo}} = 47$, derived from SDSS data.

Though a complete review of subhalo constraints on the properties of particle DM is beyond the scope of this paper, we note several important points. First, the Milky Way satellite population may not resemble that of a typical galaxy of its size and morphology, and surveys of dwarf galaxies targeting their stellar content must be corrected for completeness [42]. To address the former issue, surveys such as Satellites Around Galactic Analogues [43] aim to study the satellites of Milky Way analogues in the local Universe. Recent gravitational lensing surveys have also provided strong constraints on the properties of low-mass (down to $\lesssim 10^8 M_{\odot}$) subhaloes at cosmological redshifts unbiased by the haloes' stellar content [44-54]. In all of these cases, constraining m_{γ} using structure observables both simulated and observed—also requires a model of the DM power spectrum, which is affected by its production mechanism, with all of the sources of uncertainty discussed in the previous paragraph [55–58].

Space-based x-ray observatories such as HEAO-1 [59], Chandra [60.61], XMM-Newton [59.62–64], Suzaku [39,65], Fermi-GBM [40], and INTEGRAL [41,66] have provided the most robust constraints on the $\chi \rightarrow \nu + \gamma$ decay rate for $m_{\chi} \simeq 1-100$ keV. The observation of an unknown x-ray line at $E \simeq 3.5$ keV ("the 3.5-keV line") in several analyses [34–36] has led to much interest, as well as many follow-up analyses using different instruments and astrophysical targets [30,38,39,63,64,67-83]. Some suggest that the 3.5-keV line may be a signature of sterileneutrino DM [84] or other DM candidates [85-89]; alternatively, modeling systematics [69,71] or novel astrophysical processes [90,91] may play a role. Future highspectral-resolution x-ray instruments may also be able to investigate the DM hypothesis for the origin of the 3.5-keV signal via velocity spectroscopy [92,93].

Since its launch in 2012, the NuSTAR observatory, due to its unique large-angle aperture for unfocused x-rays, has provided the leading constraints on sterile-neutrino DM across the mass range 10-50 keV, leveraging observations of the Bullet Cluster [30], blank-sky fields [32], the Galactic center [31], and the M31 galaxy [33]. In each of these cases, the NuSTAR observations were originally performed to study non-DM phenomena; therefore, DM searches using these data had to contend with large astrophysical backgrounds and/or reduced effective areas from masking bright point sources in the field of view (FOV). Improving upon these constraints, and extending them to the NuSTAR limit of E = 3 keV (e.g., to test the tentative 3.5-keV signal), will therefore require observations with lower astrophysical backgrounds, as well as an improved model of the low-energy NuSTAR instrumental background.

In this paper, we present new constraints on the decay rate of sterile-neutrino DM particles using two NuSTAR observations, one $\sim 10^{\circ}$ above and the other $\sim 10^{\circ}$ below the Galactic plane, chosen to minimize astrophysical x-ray

emission while still remaining near the center of the Galactic DM halo. These are the first NuSTAR observations dedicated to DM searches.

In Sec. II, we describe the data reduction and spectral modeling of the NuSTAR data, consistently incorporating the flux from the focused and unfocused FOVs. In Sec. III, we combine the line flux limits from these new observations to constrain the $\chi \to \nu + \gamma$ decay rate for sterile neutrinos in the mass range 10–40 keV, obtaining the strongest constraints to date in the 10–12 keV mass range. We conclude in Sec. IV.

II. NUSTAR DATA ANALYSIS

In this section, we outline the aspects of the NuSTAR instrument that are relevant to our DM search, and describe NuSTAR's unique wide-angle aperture for unfocused x-rays (Sec. II A). After describing the recent NuSTAR off-plane observations (Sec. II B) and our treatment of the NuSTAR instrument response (Sec. II C), we conclude with a discussion of the spectral model we use to analyze the data (Sec. II D).

A. The NuSTAR instrument

The NuSTAR instrument is more fully described in Refs. [94–96], with the aspects of the instrument relevant for our search technique described in our previous papers [31,33]. Here, we summarize several key aspects.

The NuSTAR instrument contains two identical, independent, and coaligned telescopes, each consisting of a grazing-incidence Pt/C-coated x-ray optics module and a focal plane module (FPM). The FPMs (labeled A and B) contain an aperture stop, a ~100-µm beryllium x-ray window with energy-dependent transmission efficiency $\mathcal{E}_{\text{Be}}(E)$, and a solid-state CdZnTe detector array with energy resolution ~0.4 keV for x-rays with energies $E \lesssim 20$ keV. Within the telescopes, properly-focused incoming x-rays reflect twice off the mirror segments, leading to their alternative name of 2-bounce (2b) photons. Both telescopes share essentially-overlapping $13' \times 13'$ FOVs for focused x-rays with energies between 3–79 keV. The lower limit is primarily set by inactive material on the surface of the detector and $\mathcal{E}_{\mathrm{Be}}(E)$ (see Secs. II C and II D), whereas the upper limit is set by the Pt K-edge of the mirror materials. The maximum x-ray energy recorded by the detectors is \sim 160 keV.

Unlike previous focusing x-ray telescopes such as Chandra or XMM-Newton, the 10-m gap between the NuSTAR optics bench and the focal plane is open to the sky, allowing stray photons to strike the detector array without interacting with the mirror elements or being blocked by the aperture stops. For this reason, these unfocused x-rays are called 0-bounce (0b) photons. Although the 0-bounce effective area A_{0b} is limited by the physical ~13 cm² area of each detector array, the effective 0-bounce FOV $\Delta\Omega_{0b}$ subtended by each array is $\sim 4.5 \text{ deg}^2$, nearly two orders of magnitude larger than the 2-bounce FOV $\Delta\Omega_{2b}$, and more than counterbalancing the factor of ~20 reduction in effective area between the 2-bounce and 0-bounce apertures. This approach provides a large increase in sensitivity to diffuse x-ray emission such as that expected from decaying DM in galactic halos, and thus the 0-bounce technique has been the dominant contribution to recent NuSTAR sterile-neutrino constraints [31–33].

B. NuSTAR faint-sky off-plane observations

The previous NuSTAR sterile-neutrino search in the Galactic center region [31] was hampered by the presence of bright x-ray point sources in both the 0-bounce and 2-bounce FOVs, whose removal from the data greatly reduced the effective area, as well as a large continuum background from the Galactic ridge x-ray emission (GRXE, see Sec. II D) which was the dominant background component for $E \lesssim 20$ keV. To combat both of these issues, we designed two dedicated NuSTAR observations (see Table I), one $\sim 10^{\circ}$ above the Galactic plane (obsID 40410001002), and the other $\sim 10^{\circ}$ below (40410002002). The high Galactic latitude of these fields was chosen to minimize the GRXE continuum background while still remaining near the center of the Galactic DM halo, as well as avoiding known bright x-ray sources near the Galactic plane (see Fig. 2).

The NuSTAR observations described above were carried out in August and October 2018, with an initial unfiltered exposure time of ~200 ks (summed over both obsIDs and FPMs). Data reduction and analysis are performed using the NuSTAR Data Analysis Software pipeline, NUSTARDAS V1.5.1. The flags SAAMODE=OPTIMIZED and TENTACLE=YES are used to remove events coincident with NuSTAR

TABLE I. NuSTAR Galactic bulge observations used in this analysis, with 0-bounce effective areas after data cleaning.

NuSTAR	Pointing (J2000)	Effective Exposure ^a FPMA/B (ks)	Detector Area A_{0b}^{b}	Solid Angle $\Delta\Omega_{0b}^{c}$
obsID	RA, Dec (deg)		FPMA/B (cm ²)	FPMA/B (deg ²)
40410001002	253.2508, -26.6472	50.0/49.8	11.97/11.88	4.36/4.62
40410002002	280.3521, -27.6344	44.7/44.6	12.71/12.60	4.53/4.56

^aAfter OPTIMIZED SAA filtering and manual data screening.

After bad pixel removal (both obsIDs) and point-source masking (40410001002 only).

^cAverage solid angle of sky for detecting 0-bounce photons, after correcting for bad pixel removal and vignetting efficiency.

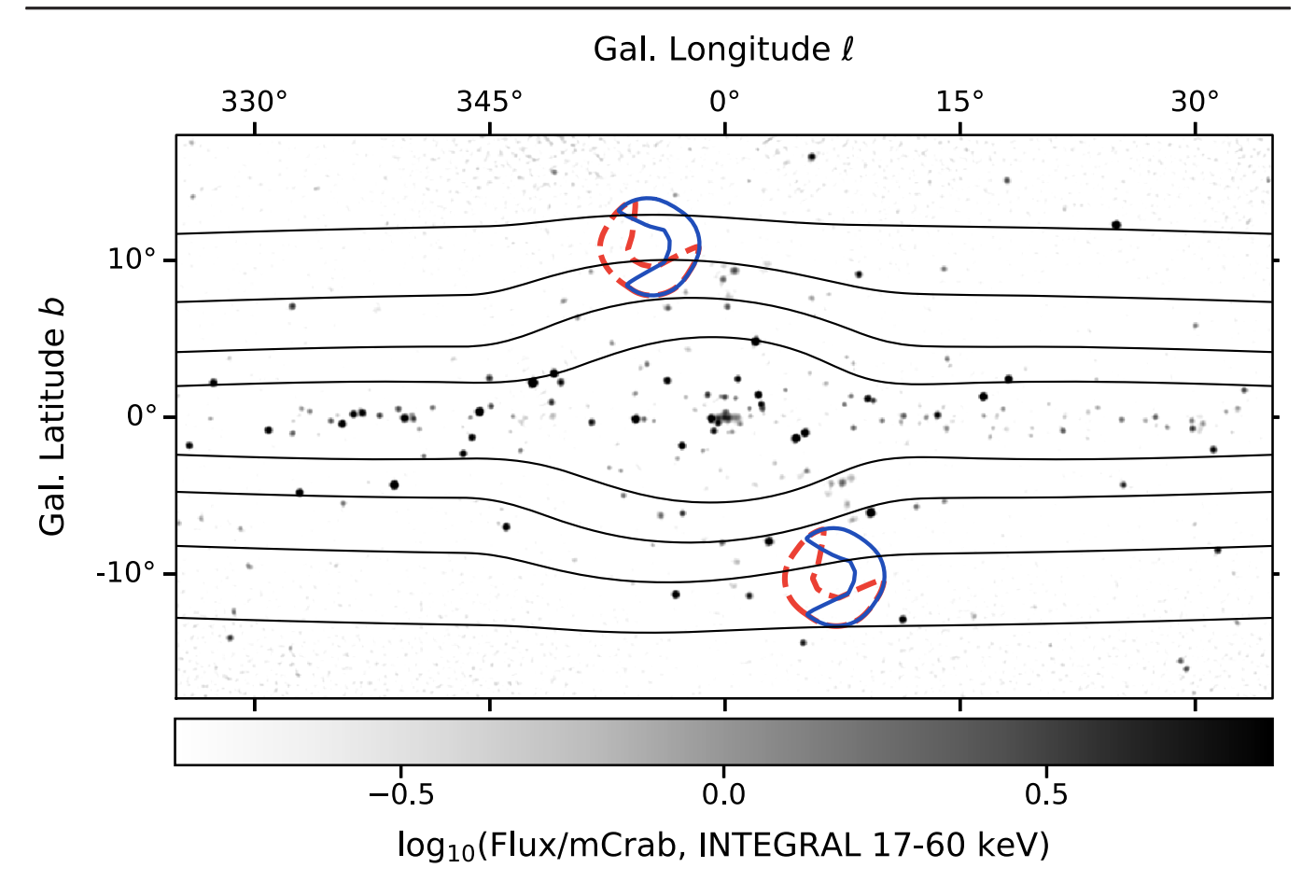


FIG. 2. Sky map of the Galactic bulge region. The base color map shows the 17–60 keV flux measured by INTEGRAL [97], with many x-ray point sources clearly visible. The 0-bounce FOVs for the observations analyzed in this paper are indicated by the dashed red (FPMA) and solid blue (FPMB) "Pac-Man"-shaped curves, and avoid known bright x-ray sources. The solid black contours indicate the predicted GRXE flux using the Galactic stellar mass model from Ref. [98] and the GRXE emissivity model from Ref. [99] (see Sec. II D). The contour values are symmetric about $b = 0^{\circ}$, decrease as |b| increases, and are evenly spaced in $\log_{10}(\text{flux})$ between $10^{-12.5}$ – 10^{-11} erg s⁻¹ cm⁻² deg⁻², inclusive.

passages through the South Atlantic Anomaly (SAA), and "bad pixels" (defined in the NuSTAR calibration database) are removed. We observe a faint x-ray point source near the edge of the 2-bounce FOV in obsID 40410001002, whose position is consistent with the chromospherically active stellar binary HD 152178 [100,101]. This system has also been detected in x-rays by RXTE [102] and Suzaku [103]. To eliminate systematic uncertainties associated with modeling this source's spectrum, we remove from our analysis all x-ray events in a circular region of radius 75" around the nominal position of the source in both FPMs, excluding \gtrsim 80% of the source photons [104]. (The position of the x-ray source 1RXS J165306.1-263434 also lies within the 2-bounce FOV of this obsID [102]; however, it is sufficiently faint that its NuSTAR spectrum is consistent with background, so we do not exclude it from the analysis. There are no x-ray point sources visible in obsID 40410002002.) Finally, we inspect the 3-10 keV light-curves of each observation to check for transient fluctuations due to solar activity or unfiltered SAA events, and remove any time

intervals with a count rate $> 2.5\sigma$ from the quiescent average. After all cuts, the total cleaned exposure time used in this analysis, summed over both obsIDs and telescopes, is \sim 190 ks.

We extract spectra from the full detector planes as extended sources using the NUPRODUCTS routine in NUSTARDAS, and bin each spectrum with equal logarithmic separations $\Delta \log_{10} E = 0.01$ (i.e., 100 bins per decade) in the energy ranges 5–20 keV and 95–110 keV. This provides a statistical uncertainty that is everywhere ~10% per bin while also being narrower than the ~0.4-keV NuSTAR energy resolution across the energy range 5-20 keV. As described in Ref. [33], we exclude the energy range 3-5 keV, as the behavior of the low-energy NuSTAR background—particularly the origin of the 3.5- and 4.5-keV lines in the default background model—is the subject of active investigation. (Additionally, including the 3-5 keV region can bias the determination of the internal power-law parameters discussed in Sec. II D; see Ref. [33] for details.) We also exclude the energy range 20–95 keV, as this region is dominated by a forest of instrumental lines. DM constraints in this energy range are therefore weakened and prone to systematic effects, as discussed in Refs. [31–33]. Excluding this energy range also speeds up our analysis, and we verify that it does not affect our results in the 5–20 keV energy range. Finally, we note that the 20–95 keV energy range has already been largely excluded by previous sterile-neutrino searches using data from Fermi-GBM [40], INTEGRAL [41], and NuSTAR [31–33].

C. NuSTAR response files

To describe the effects of the detector effective area and solid angle for the CXB, GRXE, and DM line components described in Sec. IID, we define custom response files that relate the measured event rate $d^2N/dEdt$ to the astrophysical flux. For 0-bounce components, the response is $\mathcal{E}_{\text{Be}}(E)A_{0\text{b}}\Delta\Omega_{0\text{b}}$, where the grasp $A_{0\text{b}}\Delta\Omega_{0\text{b}}$ is calculated using the NUSKYBGD code [95] and $\mathcal{E}_{\text{Be}}(E)$ is the Be window transmission efficiency. For 2-bounce components, the response is $\mathcal{E}_{\text{Be}}(E)A_{2\text{b}}(E)\Delta\Omega_{2\text{b}}$, where $\mathcal{E}_{\text{Be}}(E)$ and $A_{2b}(E)$ are calculated by NUSTARDAS, extracting the entire FOV as an extended source using NUPRODUCTS. Here, $\Delta\Omega_{2b}$ is simply the geometric area of the 2-bounce FOV, and is $\sim 0.046 \text{ deg}^2$ for obsID 40410001002 and $\sim 0.047 \text{ deg}^2$ for obsID 40410002002, the former being slightly less than the latter due to the exclusion of the 75"radius circle around the point source. The responses for internal detector components—the internal continuum, power-law, and lines—are calculated by NUPRODUCTS, and do not depend on area or solid angle.

D. NuSTAR spectral modeling

Our spectral model contains six components, which may be broadly classified as having instrumental or astrophysical origins (see Table II). The instrumental background consists of a low-energy internal power-law dominant at energies $E\lesssim 10$ keV, the internal detector continuum, and a series of phenomenologically-motivated lines. The astrophysical components include the cosmic x-ray background (CXB), with an event rate similar to the instrumental components' over the energy range of this analysis; and the GRXE, whose flux is a factor $\sim \! 10$ lower than the CXB. The treatment of each of these model components is described in this section.

To describe the internal continuum and line backgrounds, we adopt the default NuSTAR spectral model of Ref. [95]. The internal continuum is parametrized by a broken power-law with $E_{\rm break}=124~{\rm keV}$, and the line energies and widths are frozen to the values in the default model, with only the line normalizations free to fit. (The 124-keV break is outside the energy range of our analysis, and thus does not affect the fit; we include it merely for continuity with the default NuSTAR model.) The line normalizations are also allowed to vary between each of the spectra, accounting for differences in the instrumental

background conditions between the FPMs. We retain the 95–110 keV data as the event rate in this range is dominated by the internal continuum, and is necessary to constrain the overall continuum normalization. We explore alternative high-energy intervals with endpoints around 95 keV and 120 keV, and find that the fit quality is not sensitive to the precise values of the endpoints, provided the interval is sufficiently wide to constrain the internal continuum.

The default NuSTAR instrumental background model [95] includes a ~1-keV collisionally ionized plasma component (the apec model in XSPEC [110]) which is strongest for energies E < 5 keV and is believed to result from reflected solar x-rays. Unfortunately, this model provides a poor fit $(\chi^2/\text{d.o.f.} \gtrsim 1.7)$ to the observed spectrum, with the residuals indicating a clear excess in the energy range 5–10 keV. As we exclude the E < 5 keV data, we adopt the procedure described in Refs. [33,109] and replace the apec model with a power-law. For each FPM and each obsID, we use the data collected when the telescope aperture is occulted by the Earth to constrain the power-law spectral index and normalization with respect to the internal continuum. As the Earth completely fills the 0-bounce and 2-bounce apertures during occultation mode, we assume that the astrophysical components contribute negligible flux, and include only the internal detector components when modeling the occulted data. In particular, the Earth albedo flux is suppressed by at least one order of magnitude compared to the CXB and GRXE over the energy range of our analysis [111–113]. The spectral index and relative normalization of the internal power-law are frozen to their best-fit occultation-mode values during fits to the science data, shown in Figs. 3 and 4. This procedure provides a much better fit $(\chi^2/\text{d.o.f.} \lesssim 1.4)$ to the observed science-mode spectra over the energy range of our analysis; however, there are still noticeable deviations, which will be discussed later in this section, and in Sec. III B.

The cosmic x-ray background (CXB) arises from unresolved extragalactic sources, and constitutes one of the dominant irreducible NuSTAR backgrounds in both the 0-bounce and 2-bounce FOVs. As specified in the default NuSTAR background model, we parametrize the CXB spectrum with a cut-off power-law whose flux, spectral index, and e-folding energy are fixed to the values measured in similar energy ranges by HEAO-1 and INTEGRAL [105,106]; i.e., there are no free parameters in the CXB model. This choice is supported by a previous NuSTAR analysis using the 0-bounce technique, which obtained a CXB flux consistent with our adopted value [109]. We test the effect of allowing the CXB flux to vary by $\pm 10\%$ to account for cross-calibration uncertainty or the effects of cosmic variance in the $\sim 4.5 \text{ deg}^2$ FOV, as the number density of CXB sources was previously measured by NuSTAR to be $\gtrsim 100 \text{ deg}^{-2}$ [114]. We find no significant change in the fit quality. Similarly, we examine the

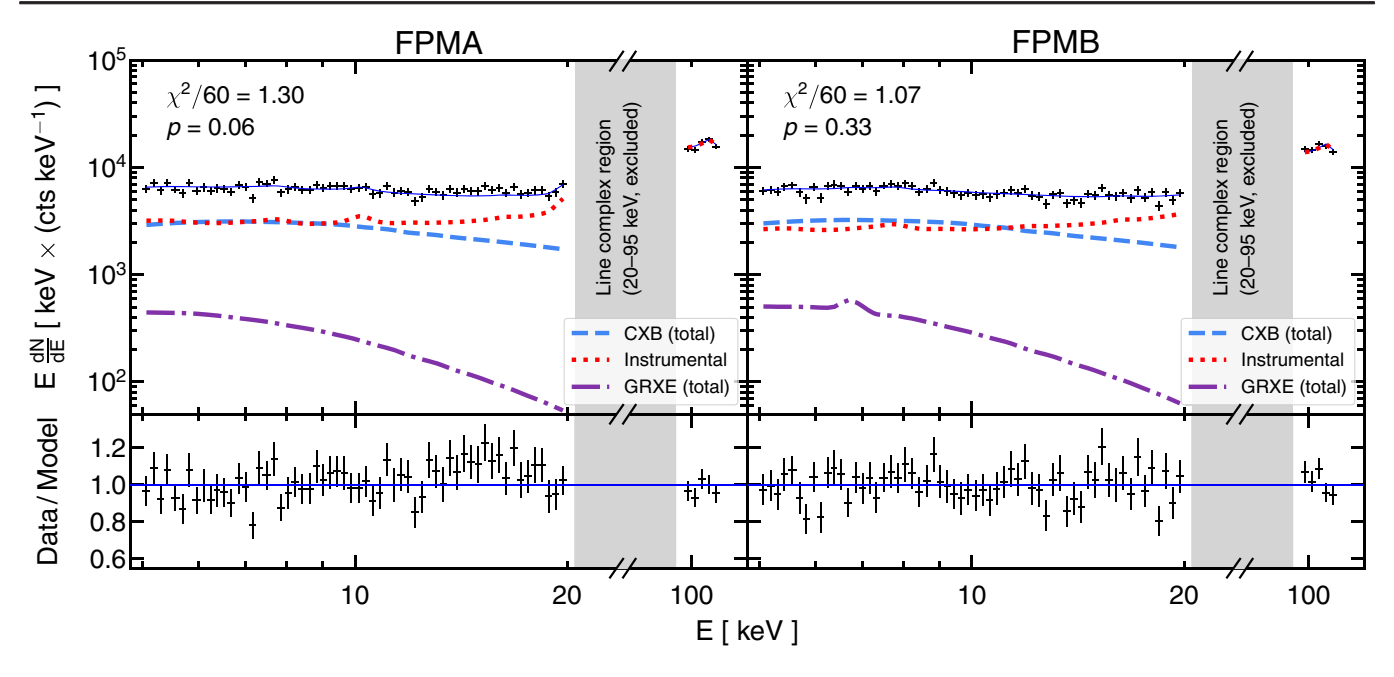


FIG. 3. Data and model spectra for obsID 40410001002, with FPMA (left) and FPMB (right), including contributions from the CXB, instrumental background, and the GRXE. The error bars correspond to $\pm 1\sigma$ statistical uncertainties, and the CXB and GRXE curves incorporate both 0-bounce and 2-bounce emission. We exclude the energy range 20–95 keV as it is dominated by internal detector lines (in previous analyses [31,33], we have already probed this range well), though we include the energy range 95–110 keV to constrain the internal detector continuum. See Sec. II D for details.

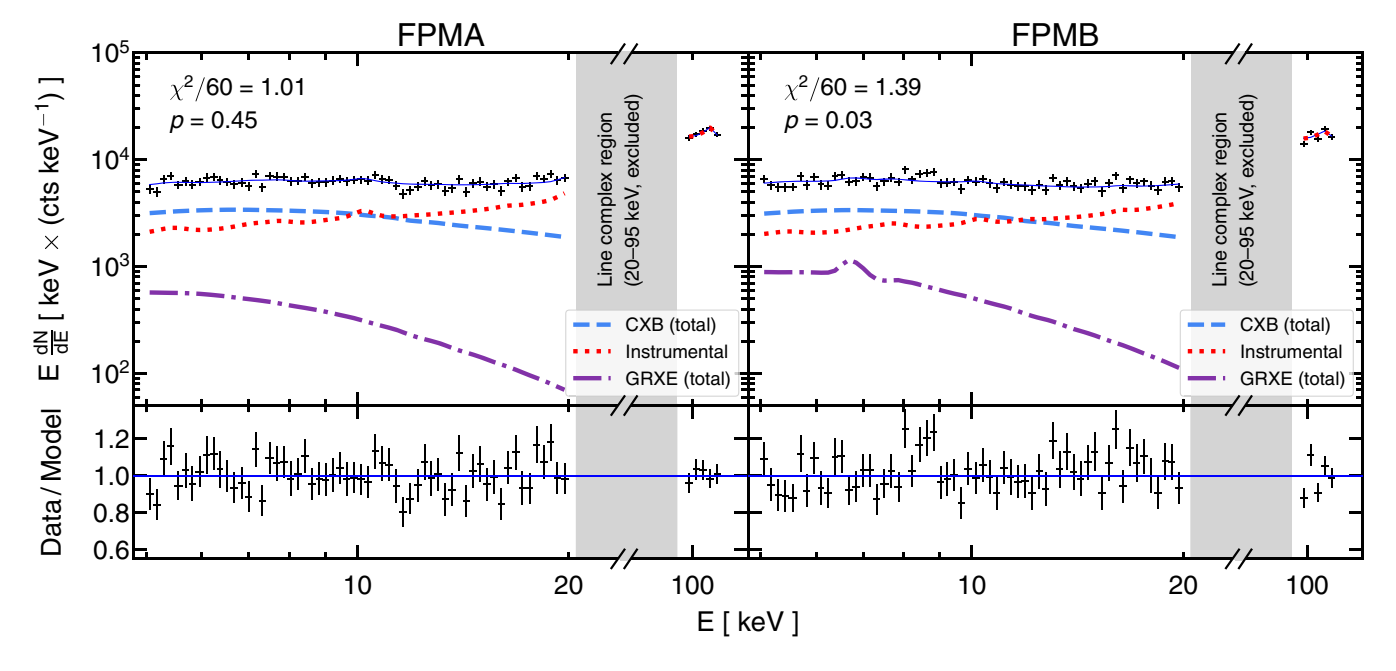


FIG. 4. Same as Fig. 3, but for obsID 40410002002.

effects of allowing the CXB spectral index to be unconstrained. In three of the spectra the best-fit CXB spectral index is consistent with our adopted value at > 90% confidence, whereas in spectrum 40410001002A the best-fit value is < 1 (inconsistent with previous measurements by HEAO-1 and INTEGRAL). The fit quality is not

significantly improved by allowing the CXB spectral index to vary in any of our spectra, so we fix it to the value in Table II. Finally, the highecut term brings a factor $\exp[(E_{\rm cut}-E)/E_{\rm fold}]$ for $E \ge E_{\rm cut}$ and is constant for $E \le E_{\rm cut}$, so we choose $E_{\rm cut}=10^{-4}$ keV to ensure that the exponential folding is applied over the full energy range

TABLE II. The NuSTAR spectral model used in this paper. Parameters with numerical values are frozen to those values, and all free parameters are allowed to vary independently between FPMA/B and between the two obsIDs.

Model component	XSPEC model ^a	Parameter	Value
CXB	powerlaw*highecut	3–20 keV flux Spectral index Γ $E_{\rm cut}$ $E_{\rm fold}$	$2.6 \times 10^{-11} \text{erg s}^{-1} \text{ cm}^{-2} \text{deg}^{-2} \text{ [105,106]}$ 1.29 [105,106] 10^{-4} keV 40 keV [105,106]
GRXE	apec	3–20 keV flux Plasma <i>kT</i> Abundance ratio	Free 8 keV [107–109] Free within 0–1.2
Internal continuum	bknpower	$E_{ m break}$ $\Gamma(E < E_{ m break})$ $\Gamma(E > E_{ m break})$ Normalization	124 keV [95] -0.05 [95] -0.85 [95] Free
Internal power-law	powerlaw	Spectral index Γ Relative norm.	Frozen for each FPM/obsID (Sec. II D) Frozen for each FPM/obsID (Sec. II D)
Internal lines	lorentz	Line energies Line widths Line norms.	10.2, 19.7, 104.5 keV [95] 0.6, 0.2, 0.5 keV [95] Free
DM line	gaussian	Line energy Line width Line flux	See Sec. II D 0 keV See Sec. II D

^aThe CXB, GRXE, and DM line models also include absorption from the interstellar medium through the tbabs model with fixed column density $N_{\rm H}$, as well as absorption from the beryllium x-ray shield. All model components except the internal continuum include the absorption effects of detector surface material. See Sec. II D for details.

of our analysis. As shown in Figs. 3 and 4, the CXB is the dominant astrophysical background in these off-plane observations.

The GRXE is believed to result from unresolved point sources in the Galactic ridge [115], and its emissivity is observed to trace the near-infrared surface brightness (and hence stellar density) of the Galaxy [99,108,116,117]. Broadband studies of the GRXE indicate that it is likely a multitemperature plasma, with $kT_1 \lesssim 1$ keV and $kT_2 \sim$ 8 keV [107,108]. We model the GRXE, which appears in both the 0-bounce and 2-bounce FOVs, as a singletemperature collisionally-ionized plasma (the apec model described previously) with a fixed temperature of 8 keV previously measured by NuSTAR; however, this analysis was not sensitive to the elemental abundances [109]. (We are unable to leave the GRXE temperature free to fit, as we find that doing so leaves the temperature almost completely unconstrained.) Particularly strong emission lines between 6–7 keV arise from $K\alpha$ transitions in neutral and highly ionized Fe, and it was these lines which limited the sensitivity of the previous NuSTAR sterile-neutrino search near the Galactic center (see Ref. [31] and Fig. 5 of this paper).

It is important to note that the "GRXE" component in our spectral model includes flux from the GRXE, un-modeled point sources, reflected x-rays from the Earth's atmo-

sphere, and any low-energy instrumental backgrounds not described by our default spectral model, as the GRXE component includes the only free normalization parameter in the low-energy part of our spectral model. Therefore, we leave both the GRXE elemental abundance (as a ratio to solar) and flux as free parameters, where the flux is unconstrained and the abundance ratio is constrained to the range 0–1.2. The 0-bounce and 2-bounce GRXE components are constrained to have the same flux and abundance ratio.

The lower bound on the GRXE abundance ratio arises from the requirement that elemental abundances be strictly positive, and the upper bound is motivated by previous measurements of the GRXE [108]. Additionally, freezing the abundance ratio to a nonzero value can force the GRXE flux to unreasonable extremes as the model attempts to fit the GRXE by way of its emission lines, thereby biasing the rest of the 5-20 keV fit. The flux of the GRXE emission lines is directly related to the number of atoms in the FOV undergoing electronic de-excitation, and hence to the elemental abundances of the plasma; as shown by the slight bump in Figs. 3 and 4, the fits to the FPMB spectra of both obsIDs prefer a slightly higher GRXE abundance ratio than the FPMA spectra, though this difference is within the uncertainty on the value of the abundance parameter.

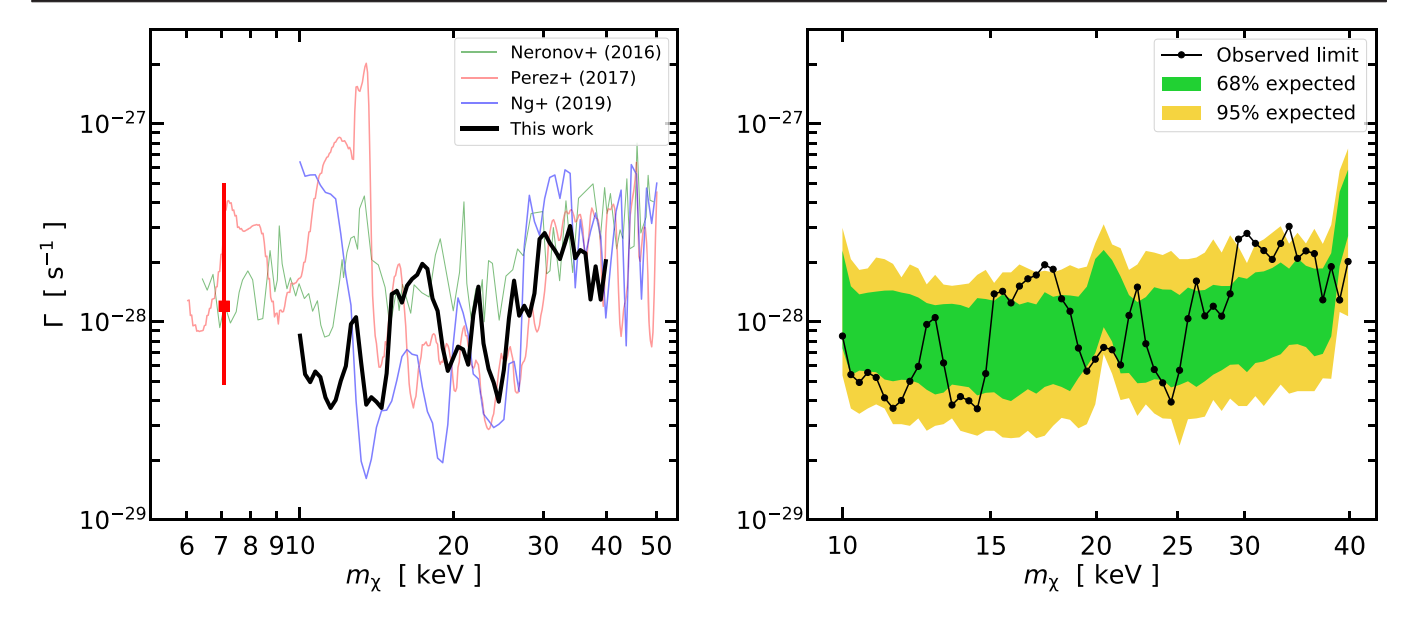


FIG. 5. Left: Comparison of the limit obtained in this paper to that from several surveys using the 0-bounce technique, including blank sky (green, Ref. [32]), Galactic center (red, Ref. [31]), and M31 fields (blue, Ref. [33]), as well as the tentative signal at $E \simeq 3.5$ keV (red point, Refs. [34–36]). With only ~190 ks, we have achieved comparable constraints to analyses with much deeper exposures [31–33]. We have achieved the best constraint in 10–12 keV mass range, essential for investigating the remaining ν MSM parameter space shown in Fig. 1. Right: The observed 95% upper limit on the DM decay rate Γ obtained in this paper, compared to the expected 68% (green) and 95% (yellow) sensitivity bands from simulations (see Sec. III B).

Finally, the freedom in the GRXE flux acts to account for any unmodeled CXB flux, as the two components have similar continuum shapes in the E < 10 keV range, where their flux is highest. By fixing the CXB and allowing the GRXE flux to float, we consistently account for any variance in the flux of both components, and we find that the best-fit GRXE flux is consistent with Galactic stellar mass and emissivity models [98,115]. Additionally, we find that allowing both the CXB and GRXE fluxes to vary leads to best-fit values which are inconsistent with the previously-described measurements of these components' flux levels.

We parameterize our DM line signal in XSPEC with a vanishingly-narrow Gaussian—i.e., a δ -function in E—as the intrinsic width of any DM line is expected to be much less than the \sim 0.4 keV detector energy resolution with which it is convolved. Our treatment of the DM line during the line-search procedure is described further in Sec. III A.

The fluxes of the astrophysical components in our spectral model—CXB, GRXE, and DM line—are attenuated by absorption and scattering in the interstellar medium (ISM). This attenuation is parametrized in terms of the equivalent column density of neutral hydrogen, $N_{\rm H}$, via the tbabs model in XSPEC [118]. We adopt fixed values of 7.0×10^{20} cm⁻² for obsID 40410001002 and 1.1×10^{21} cm⁻² for obsID 40410002002 [119,120]. (Both FPMs share the same $N_{\rm H}$ value, which is assumed to be constant across the 0-bounce and 2-bounce FOVs despite the somewhat different sky coverage and values of $\Delta\Omega_{\rm 0b}$

from A/B.) This corresponds to an optical depth $\tau \lesssim 10^{-2}$ at E=5 keV, falling steeply with increasing energy. Although the flux attenuation from the ISM is a $\lesssim 1\%$ effect across the energy range of this analysis, we include it for consistency.

Finally, we consider the absorption of x-rays within the NuSTAR instrument itself. Before incoming astrophysical x-rays (from the CXB, GRXE, or DM) strike the detectors, they must pass through a ~ 100 - μ m beryllium shield with transmission efficiency $\mathcal{E}_{\text{Be}}(E)$, rising from ~ 0.67 at E=3 keV to \sim 0.92 at E=5 keV. (The treatment of $\mathcal{E}_{\mathrm{Be}}$ is discussed further in Sec. II C.) An additional absorption effect arises in the detectors themselves. The CdZnTe detectors have a ~ 0.11 - μ m Pt contact coating, as well as a ~ 0.27 - μ m layer of inactive CdZnTe (both varying somewhat between individual detector crystals), through which incoming x-rays must pass [96]. At E = 5 keV, these detector components result in a flux attenuation of ~25%, though this decreases quickly with increasing energy [33]. These detector absorption effects (often called NUABS or DETABS) are included in every spectral component except the internal continuum.

As shown in Figs. 3 and 4, the model described in Sec. II D provides an acceptable fit to the NuSTAR spectra across most of the 5–20 keV energy range (see Figs. 3 and 4 for the reduced- χ^2 and corresponding *p*-values for each spectrum), but there are several deviations from the model that may affect our derived line flux limits, and thus require further consideration. The higher χ^2 in FPMA

of obsID 40410001002A is due to the energy range 15–20 keV (excluding this energy range yields $\chi^2/47 = 0.94$ with p = 0.59), and similarly for FPMB of obsID 40410002002B in the energy range 8–9 keV (yielding $\chi^2/54 = 1.15$ with p = 0.21). As both of these regions are excesses with respect to the default background model, the DM line flux limits in the mass ranges $m_\chi \simeq 16$ keV and 30–40 keV are correspondingly weakened (see Sec. III B), as we use a conservative line-search procedure in which the DM line flux is allowed to fill the excess (see Sec. III A). In Sec. III B, we perform Monte Carlo simulations to verify that our constraint is consistent with one limited by statistical variations in our measurement, not systematic variations due to incomplete modeling.

III. NUSTAR DM ANALYSIS

In this section, we describe the procedure used to search for DM line signals and set upper limits on the decay rate of DM to final states including a single monoenergetic photon (Sec. III A), and compare to sensitivity estimates from simulations (Sec. III B). Finally, we discuss the implications for sterile-neutrino dark matter (Sec. III C).

A. DM line search

Equipped with the spectral model described in Sec. II D, we search for DM line signals in the two observations. Our search procedure follows closely that from Refs. [31,33], and is briefly described here.

We divide the 10–40 keV mass band into bins with equal logarithmic separations $\Delta \log_{10} m_{\chi} = 0.01$ (i.e., 100 bins per decade in m_{χ}). At each mass bin, we add a DM line with photon energy $E = m_{\chi}/2$ to the model. The number of DM photons in the line for each module and observation is

$$N_{\rm DM} = \frac{\Gamma}{4\pi m_{\chi}} T A_{0\rm b} \Delta \Omega_{0\rm b} \mathcal{J} (1 + f_{2\rm b}), \tag{1}$$

where Γ is the decay rate, m_χ is the DM mass, T is the observation time, A_{0b} and $\Delta\Omega_{0b}$ are the 0-bounce effective area and effective FOV defined in Sec. II C, $\mathcal J$ is the FOV-averaged line-of-sight integral of the DM density (J-factor), and f_{2b} is the energy-dependent contribution from the 2-bounce component (see Fig. 3 in Ref. [33] for the energy dependence of the 2-bounce contribution; in this work, we find a modest ~20% enhancement at $E=10~{\rm keV}$).

To obtain the J-factors, we consider several DM density profiles. One popular choice is the generalized Navarro-Frenk-White (NFW) profile, $\rho \propto (r/r_s)^{-\gamma}(1+r/r_s)^{\gamma-3}$. For the standard (DM-only) NFW profile, we adopt an inner slope $\gamma=1$ and scale radius $r_s=20$ kpc [121,122]. We fix the galactocentric solar radius and the local DM density to be 8 kpc and 0.4 GeVcm⁻³, respectively [123–125]. The standard NFW profile was found to be a good fit to the Milky Way kinematic data [126], but it has been

suggested that the density profiles could be flattened below 1.5 kpc [127,128]. Therefore, we also consider the more conservative choice, coreNFW, where we set a density core below 1.5 kpc—i.e., $\rho(r < 1.5 \text{kpc}) = \rho(1.5 \text{kpc})$. Another conservative NFW variant we consider is the sNFW, where we use a shallower index $\gamma = 0.7$ [123]. We use sNFW as our default result, obtaining $\mathcal{J} \simeq 20 \text{ GeV cm}^{-3} \text{ kpc sr}^{-1}$ for the observation regions in this analysis; for NFW and coreNFW, the J-factors are larger by $\sim 20\%$.

Another shallow density profile often considered in the literature is the Burkert profile $\rho \propto (1+r/r_s)^{-1}(1+r^2/r_s^2)^{-1}$ [129], with best-fit local DM density \sim 0.5 GeV cm⁻³ and scale radius \sim 8 kpc [126,130]. This profile effectively has a density core within r_s , which we note is much larger than what was found in Refs. [127,128]. Even in this case, the J-factor is only \sim 10% smaller than our default sNFW choice. This small deviation shows the robustness of our results, and reflects an additional advantage of using observations slightly offset from the Galactic center.

At each DM mass, the only free parameter for the DM line is the decay rate. We find the best-fit $\chi^2(\Gamma)$ distribution for each module and observation by scanning through a range of Γ , refitting the entire spectral model to find the minimum χ^2 value for each Γ . This line-search procedure is conservative, as it allows the DM line to attain the full strength of any background lines.

The sensitivity of the two observations (four separate fits including both modules) at each m_{χ} are combined by adding the respective χ^2 distributions:

$$X^{2}(\Gamma) = \sum_{\text{obs}} \chi^{2}(\Gamma). \tag{2}$$

We note that for each module, the background parameters are allowed to be independent (see Sec. II D for exceptions). Compared with simply stacking the spectra, this combining procedure is used to avoid potential systematic errors due to combining observations with different instrumental and/or astrophysical backgrounds.

The minimum in $X^2(\Gamma)$ for each mass bin corresponds to the best-fit decay rate Γ_{\min} , with a 5σ line detection requiring $X^2(\Gamma_{\min}) - X^2(\Gamma = 0) < -25$. We find no signals consistent with decaying DM in the mass range 10–40 keV, and instead set upper limits on the DM decay rate. The 95% one-sided upper limit, Γ_{95} , occurs at $X^2(\Gamma_{95}) = X^2(\Gamma_{\min}) + 2.71$, and is shown in both frames of Fig. 5. In the 10–40 keV mass range, our results are comparable to previous NuSTAR limits from blank-sky [32], Galactic center [31], and M31 observations [33]. In particular, we are able to improve upon previous constraints in the 10–12 keV mass range by a factor of \sim 2. Finally, we note that with only \sim 190 ks exposure, our dedicated Galactic bulge observations are able to achieve sensitivity comparable with searches using several

Ms combined exposure. This is due to the low astrophysical background, as well as the large J-factors in the chosen FOVs.

B. Sensitivity estimation with simulations

To validate our results, we perform line searches in mock spectra to find the expected upper limits when the spectra are purely statistically limited. This exercise also allows us to further study the deviations discussed in Sec. II D.

Instead of fully mimicking the actual analysis, where we analyze each module separately and then combine the constraints, we simplify the procedure by considering a single spectrum (rather than all four) per mock analysis to speed up the computation. We generate 100 Monte Carlo (MC) spectra with no DM line, using the FAKEIT tool in XSPEC. Each spectrum has 200 ks exposure, and is generated using the best-fit spectral model of FPMA, obsID 40410001002. This simplification is motivated by the fact that the spectrum for each module has similar bestfit model parameters, and hence statistics. We also test the results obtained with 10 of these simplified simulations against 10 full realizations (i.e., including both obsIDs and both FPMs) and find good agreement. We then pass these mock spectra through the same fitting and line-search procedure as the data. At each mass bin, we thus have 100 simulated upper limits. We interpolate the cumulative distribution of these upper limits and find the corresponding 68% and 95% intervals. The upper limits can then obtained directly from the line-search procedure (see Sec. III A) without needing to combine different FPMs.

The right panel of Fig. 5 shows the expected upper limit bands obtained with the mock spectra. Our upper limits obtained from real data are consistent with the MC expectation across most of the 10–40 keV mass range at the 2σ level; however, there are several features that warrant closer attention.

As described in Sec. II D, the high χ^2 values for spectra 40410001002A and 40410002002B are caused primarily by isolated excesses in the energy ranges $\sim 15-20 \text{ keV}$ and ~8–9 keV, respectively. We first consider the possibility of these excesses being purely statistical. Though the corresponding p-values are small—0.06 and 0.03, respectively—this possibility is supported by these excesses appearing in only two of the spectra, and in two different energy ranges. Additionally, the upward fluctuations in the observed limit lie within the 95% band expected from MC simulations incorporating only statistical fluctuations (see the right panel of Fig. 5). If we consider the extreme procedure of excluding the energy ranges 15-20 keV and 8-9 keV in spectra 40410001002A and 40410002002B, respectively, the DM limits in the mass ranges \sim 16–18 keV and ~30-40 keV are strengthened by a factor ~1.3, as we are no longer including data which favor nonzero DM flux; excluding these excesses also reduces the best-fit continuum level over the rest of the energy range, slightly weakening the overall limit elsewhere by at most a factor ~ 1.5 . In both cases, the changes in the DM limit are well within the MC band of Fig. 5, so we do not pursue the extreme procedure of excluding these energy ranges from our analysis *a posteriori*.

We also test the effect of incorporating a flat 7.5% systematic across the entire energy range of all four spectra, sufficient to give $\chi^2/60 \lesssim 1$ for each. We run these spectra through the same line-search procedure as our default analysis, and find a combined DM limit that is a factor \sim 1.5 weaker than our default result, but still a factor \sim 1.5 stronger than the previously-leading Ref. [32] in the mass range 10–12 keV. We conclude that any systematic effects on our final DM limit are subdominant to the range expected from statistical fluctuations already shown in the right panel of Fig. 5. Adding such a flat systematic to all four spectra is also an extreme procedure considering the two spectra lacking these excesses (40410001002B and 40410002002A), as well as the isolated energy ranges in which these excesses appear; therefore, we do not apply such a flat systematic when calculating our default DM limit.

It is plausible that the excesses described previously result from some unmodeled, transient background component. Such a component was not evident during our initial data screening (see Sec. II B), but there known issues with the default NuSTAR background model in these regions. (As noted previously, the excesses in the 8–9 keV and 15–20 keV energy ranges are inconsistent with DM.) If we were to add additional background components in these regions, our DM limit in those regions would become stronger, as some of the flux assigned to the DM line would instead be incorporated into the new background components. Elucidating the form of these additional background components—if they exist—is beyond the scope of this work, and will require analysis (ongoing) of NuSTAR datasets with significantly longer exposure time

We conclude by considering the ranges where the DM limit in Fig. 5 most departs from the MC expectation, though in all cases the observed limit remains consistent with the 95% MC band. (The upward fluctuations in the observed limit near masses ~16-18 keV and ~30-40 keV have already been discussed.) First, the upward fluctuations near the edges of the region of interest (masses 10 keV and 40 keV) likely arise from parts of the DM line leaving the energy range 5–20 keV. Second, the upward fluctuation in the MC band near $m_{\gamma} \simeq 20 \text{ keV}$ is attributed to a weak line near $E \simeq 10 \text{ keV}$ in the background model, whereas the observed limit exhibits a downward fluctuation due to negative residuals in spectrum 40410001002B at $E \simeq 10$ keV. Finally, we turn to the mass range ~10-12 keV, where our results improve the most compared to previous analyses and the observed limit also touches the lower end of the MC band. A closer inspection shows that this is driven by several downward-fluctuating data points from 40410001002A and 40410002002A/B. These negative residuals appear at different energies in three different modules, and the bin widths are a factor ~4 narrower than the detector energy resolution. This lends support to the strong limit being caused by statistical downward fluctuations.

C. Sterile-neutrino DM constraints

For sterile-neutrino DM, we convert the decay rate constraints to mixing angle constraints using [17,18]

$$\Gamma = 1.38 \times 10^{-32} \,\mathrm{s}^{-1} \left(\frac{\sin^2 2\theta}{10^{-10}} \right) \left(\frac{m_{\chi}}{\mathrm{keV}} \right)^5.$$
 (3)

The aggregate constraints in the mass-mixing-angle plane from x-ray searches (including NuSTAR) are shown in Fig. 1. As described previously, our high-latitude Galactic bulge constraints are a factor ~2 stronger than the previous leading limits [32] in the mass range 10–12 keV while requiring a factor ~50 less exposure time, and are comparable with previous NuSTAR constraints over the rest of the 10–40 keV mass range. This supports the use of observation regions with low astrophysical background and large J-factors.

In the context of the ν MSM, the parameter space is also bounded by production and structure formation constraints [26,28] (see also Ref. [33] for discussion). As discussed in Sec. III B, the DM line analysis in this paper is limited mostly by statistics, except for the known feature near $E \simeq 15$ keV. To cover the ν MSM window for $m_{\gamma} > 10$ keV, a factor ~4 improvement in sensitivity is needed, corresponding to ~4 Ms exposure of regions with large J-factors and minimal astrophysical backgrounds (similar to the present paper). Though a survey of this depth is feasible, we caution that systematic deviations from the default NuSTAR background model will likely prevent long exposures from reaching their design sensitivity until an improved model of the NuSTAR instrumental background can be developed. Ongoing work for improving the NuSTAR instrumental background model, especially in the 3-5 keV energy range, will be essential for further testing of the ν MSM down to $m_{\gamma} = 6$ keV, including the tentative signal at $E \simeq 3.5$ keV.

IV. CONCLUSIONS AND OUTLOOK

The NuSTAR observatory's large FOV for unfocused x-rays has been pivotal in constraining the properties of sterile-neutrino DM with $m_{\chi} \sim \text{keV}$, such as that predicted by the ν MSM. NuSTAR observations of the Galactic center, blank-sky extragalactic fields, and M31 have provided world-leading constraints on the $\chi \rightarrow \nu + \gamma$ decay rate in the mass range 10–50 keV, practically closing the "window" in the ν MSM parameter space for masses

20–50 keV. Closing the window for masses 6–20 keV, however, has proved difficult, due to large astrophysical x-ray backgrounds in the observation regions.

In this paper, we analyze a combined ~190 ks of NuSTAR observations to search for x-rays originating from the radiative decay of sterile-neutrino DM in the Galactic halo. The observation regions were optimized to reduce astrophysical x-ray backgrounds from Galactic x-ray sources and from the Galactic ridge x-ray emission while remaining near the center of the Galactic halo, where the DM decay signal is expected to be strongest. We consistently model the flux from both the focused (2-bounce) and unfocused (0-bounce) NuSTAR apertures, though our sensitivity to decaying DM is dominated by the large unfocused FOV. To avoid the systematic effects of stacking spectra with different instrumental and astrophysical backgrounds, we model the spectra individually and combine the sensitivity of each.

Finding no evidence of sterile-neutrino DM decays, we instead set upper limits on the sterile neutrino decay rate in the mass range 10–40 keV. In the mass range ~ 10 –12 keV, our limits are a factor ~ 2 stronger than the previous leading limits while requiring a factor ~ 50 less exposure time. This is due in part to the low astrophysical background and large J-factor in these optimized observation regions, as well as downward statistical fluctuations. We also perform Monte Carlo simulations to determine our expected DM sensitivity, and find that our derived limits are consistent with expectations across most of the 10–40 keV mass range.

As the astrophysical background (now dominated by the irreducible CXB flux) in these observations is comparable to the instrumental background, we observe deviations of the spectra from the default NuSTAR background model, particularly in the energy ranges \sim 8–9 keV and \sim 15–20 keV. Though similar effects are visible in other NuSTAR analyses (see the left panel of Fig. 5), the excesses in our spectra are consistent with statistical fluctuations (see Sec. III B). Detailed characterization of the instrumental background is ongoing, and additional NuSTAR searches, particularly with an improved model of the instrumental background, will be uniquely suited to probing the remaining ν MSM parameter space, as well as investigating the nature of the 3.5-keV line.

ACKNOWLEDGMENTS

We thank Alexey Boyarsky, Steve Rossland, Oleg Ruchayskiy, and Shuo Zhang for helpful comments and discussions. The NuSTAR observations described in this work were awarded under NASA Grant No. 80NSSC18K1615. We thank the NuSTAR team at NASA, JPL, and CalTech for the excellent performance of the instrument and their assistance with initial data processing. The computational aspects of this work made extensive use of the following packages: SAOIMAGE DS9 distributed by the Smithsonian

Astrophysical Observatory; the SCIPY ecosystem [131], particularly MATPLOTLIB and NUMPY; and ASTROPY, a community-developed core PYTHON package for Astronomy [132,133]. This research has made use of data and software provided by the High Energy Astrophysics Science Archive Research Center (HEASARC), which is a service of the Astrophysics Science Division at NASA/GSFC and the High Energy Astrophysics Division of the Smithsonian Astrophysical Observatory. B. M. R. and K. P. receive support from NASA Grant No. 80NSSC18K1615. B. M. R. is also partially supported by MIT Department of Physics and

School of Science fellowships. K. C. Y. N. is supported by a Croucher Fellowship and a Benoziyo Fellowship. K. P. receives additional support from the Alfred P. Sloan Foundation and RCSA Cottrell Scholar Award No. 25928. J. F. B. is supported by NSF Grant No. PHY-1714479. S. H. is supported by the U.S. Department of Energy under Award No. DE-SC0018327, as well as NSF Grants No. AST-1908960 and No. PHY-1914409. R. K. receives support from the Russian Science Foundation under Grant No. 19-12-00396. D. R. W. is supported by NASA ADAP Grant No. 80NSSC18K0686.

- [1] M. Tanabashi *et al.* (Particle Data Group), Review of particle physics, Phys. Rev. D **98**, 030001 (2018).
- [2] G. Bertone, D. Hooper, and J. Silk, Particle dark matter: Evidence, candidates and constraints, Phys. Rep. 405, 279 (2005).
- [3] L. E. Strigari, Galactic searches for dark matter, Phys. Rep. **531**, 1 (2013).
- [4] M. S. Seigar, *Dark Matter in the Universe* (Morgan & Claypool Publishers, San Rafael, California, 2015).
- [5] M. R. Buckley and A. H. G. Peter, Gravitational probes of dark matter physics, Phys. Rep. 761, 1 (2018).
- [6] N. Aghanim *et al.* (Planck Collaboration), Planck 2018 results. VI. Cosmological parameters, arXiv:1807. 06209.
- [7] R. H. Wechsler and J. L. Tinker, The connection between Galaxies and their dark matter Halos, Annu. Rev. Astron. Astrophys. **56**, 435 (2018).
- [8] J. M. Gaskins, A review of indirect searches for particle dark matter, Contemp. Phys. **57**, 496 (2016).
- [9] T. Asaka, S. Blanchet, and M. Shaposhnikov, The νMSM, dark matter and neutrino masses, Phys. Lett. B **631**, 151 (2005).
- [10] T. Asaka, M. Laine, and M. Shaposhnikov, Lightest sterile neutrino abundance within the νMSM, J. High Energy Phys. 01 (2007) 091; 02 (2015) 28.
- [11] L. Canetti, M. Drewes, T. Frossard, and M. Shaposhnikov, Dark matter, baryogenesis and neutrino oscillations from right handed neutrinos, Phys. Rev. D 87, 093006 (2013).
- [12] L. Canetti, M. Drewes, and M. Shaposhnikov, Sterile Neutrinos as the Origin of Dark and Baryonic Matter, Phys. Rev. Lett. 110, 061801 (2013).
- [13] A. Kusenko, Sterile neutrinos: The dark side of the light fermions, Phys. Rep. **481**, 1 (2009).
- [14] R. Adhikari *et al.*, A white paper on keV sterile neutrino dark matter, J. Cosmol. Astropart. Phys. 01 (2017) 025.
- [15] K. N. Abazajian, Sterile neutrinos in cosmology, Phys. Rep. **711–712**, 1 (2017).
- [16] A. Boyarsky, M. Drewes, T. Lasserre, S. Mertens, and O. Ruchayskiy, Sterile neutrino dark matter, Prog. Part. Nucl. Phys. 104, 1 (2019).
- [17] R. Shrock, Decay $L^0 \rightarrow \nu_l \gamma$ in gauge theories of weak and electromagnetic interactions, Phys. Rev. D **9**, 743 (1974).

- [18] P. B. Pal and L. Wolfenstein, Radiative decays of massive neutrinos, Phys. Rev. D 25, 766 (1982).
- [19] A. D. Dolgov and S. H. Hansen, Massive sterile neutrinos as warm dark matter, Astropart. Phys. 16, 339 (2002).
- [20] K. Abazajian, G. M. Fuller, and W. H. Tucker, Direct detection of warm dark matter in the x-ray, Astrophys. J. 562, 593 (2001).
- [21] S. Dodelson and L. M. Widrow, Sterile Neutrinos as Dark Matter, Phys. Rev. Lett. 72, 17 (1994).
- [22] X.-D. Shi and G. M. Fuller, A New Dark Matter Candidate: Nonthermal Sterile Neutrinos, Phys. Rev. Lett. 82, 2832 (1999).
- [23] A. D. Dolgov, S. H. Hansen, S. Pastor, S. T. Petcov, G. G. Raffelt, and D. V. Semikoz, Cosmological bounds on neutrino degeneracy improved by flavor oscillations, Nucl. Phys. B632, 363 (2002).
- [24] P. D. Serpico and G. G. Raffelt, Lepton asymmetry and primordial nucleosynthesis in the era of precision cosmology, Phys. Rev. D 71, 127301 (2005).
- [25] A. Boyarsky, O. Ruchayskiy, and M. Shaposhnikov, The role of sterile neutrinos in cosmology and astrophysics, Annu. Rev. Nucl. Part. Sci. **59**, 191 (2009).
- [26] T. Venumadhav, F.-Y. Cyr-Racine, K. N. Abazajian, and C. M. Hirata, Sterile neutrino dark matter: Weak interactions in the strong coupling epoch, Phys. Rev. D 94, 043515 (2016).
- [27] M. Laine and M. Shaposhnikov, Sterile neutrino dark matter as a consequence of *ν*MSM-induced lepton asymmetry, J. Cosmol. Astropart. Phys. 806 (2008) 031.
- [28] J. F. Cherry and S. Horiuchi, Closing in on resonantly produced sterile neutrino dark matter, Phys. Rev. D 95, 083015 (2017).
- [29] J. Ghiglieri and M. Laine, Improved determination of sterile neutrino dark matter spectrum, J. High Energy Phys. 11 (2015) 171.
- [30] S. Riemer-Sørensen *et al.*, Dark matter line emission constraints from NuSTAR observations of the bullet cluster, Astrophys. J. **810**, 48 (2015).
- [31] K. Perez, K. C. Y. Ng, J. F. Beacom, C. Hersh, S. Horiuchi, and R. Krivonos, Almost closing the *ν*MSM sterile neutrino dark matter window with NuSTAR, Phys. Rev. D **95**, 123002 (2017).

- [32] A. Neronov, D. Malyshev, and D. Eckert, Decaying dark matter search with NuSTAR deep sky observations, Phys. Rev. D 94, 123504 (2016).
- [33] K. C. Y. Ng, B. M. Roach, K. Perez, J. F. Beacom, S. Horiuchi, R. Krivonos, and D. R. Wik, New constraints on sterile neutrino dark matter from NuSTAR M31 observations, Phys. Rev. D 99, 083005 (2019).
- [34] A. Boyarsky, O. Ruchayskiy, D. Iakubovskyi, and J. Franse, Unidentified Line in X-Ray Spectra of the Andromeda Galaxy and Perseus Galaxy Cluster, Phys. Rev. Lett. **113**, 251301 (2014).
- [35] E. Bulbul, M. Markevitch, A. Foster, R. K. Smith, M. Loewenstein, and S. W. Randall, Detection of an unidentified emission line in the stacked x-ray spectrum of Galaxy clusters, Astrophys. J. 789, 13 (2014).
- [36] A. Boyarsky, J. Franse, D. Iakubovskyi, and O. Ruchayskiy, Checking the Dark Matter Origin of a 3.53 keV Line with the Milky Way Center, Phys. Rev. Lett. **115**, 161301 (2015).
- [37] S. Horiuchi, B. Bozek, K. N. Abazajian, M. Boylan-Kolchin, J. S. Bullock, S. Garrison-Kimmel, and J. Onorbe, Properties of resonantly produced sterile neutrino dark matter subhaloes, Mon. Not. R. Astron. Soc. 456, 4346 (2016).
- [38] O. Ruchayskiy, A. Boyarsky, D. Iakubovskyi, E. Bulbul, D. Eckert, J. Franse, D. Malyshev, M. Markevitch, and A. Neronov, Searching for decaying dark matter in deep XMM–Newton observation of the Draco Dwarf spheroidal, Mon. Not. R. Astron. Soc. 460, 1390 (2016).
- [39] T. Tamura, R. Iizuka, Y. Maeda, K. Mitsuda, and N. Y. Yamasaki, An x-ray spectroscopic search for dark matter in the Perseus cluster with Suzaku, Publ. Astron. Soc. Jpn. 67, 23 (2015).
- [40] K. C. Y. Ng, S. Horiuchi, J. M. Gaskins, M. Smith, and R. Preece, Improved limits on sterile neutrino dark matter using full-sky Fermi Gamma-ray Burst Monitor data, Phys. Rev. D 92, 043503 (2015).
- [41] A. Boyarsky, D. Malyshev, A. Neronov, and O. Ruchayskiy, Constraining dark matter properties with SPI, Mon. Not. R. Astron. Soc. 387, 1345 (2008).
- [42] S. Y. Kim, A. H. G. Peter, and J. R. Hargis, Missing Satellites Problem: Completeness Corrections to the Number of Satellite Galaxies in the Milky Way are Consistent with Cold Dark Matter Predictions, Phys. Rev. Lett. 121, 211302 (2018).
- [43] M. Geha *et al.*, The SAGA survey. I. Satellite Galaxy populations around eight Milky Way analogs, Astrophys. J. 847, 4 (2017).
- [44] L. V. E. Koopmans, Gravitational imaging of cold dark matter substructures, Mon. Not. R. Astron. Soc. 363, 1136 (2005).
- [45] S. Vegetti and L. V. E. Koopmans, Bayesian strong gravitational-lens modelling on adaptive grids: Objective detection of mass substructure in Galaxies, Mon. Not. R. Astron. Soc. **392**, 945 (2009).
- [46] S. Vegetti, O. Czoske, and L. V. E. Koopmans, Quantifying Dwarf satellites through gravitational imaging: The case of SDSS J120602.09+514229.5, Mon. Not. R. Astron. Soc. 407, 225 (2010).

- [47] S. Vegetti, L. V. E. Koopmans, A. Bolton, T. Treu, and R. Gavazzi, Detection of a dark substructure through gravitational imaging, Mon. Not. R. Astron. Soc. 408, 1969 (2010).
- [48] S. Vegetti, D. Lagattuta, J. McKean, M. W. Auger, C. D. Fassnacht, and L. V. E. Koopmans, Gravitational detection of a low-mass dark satellite galaxy at cosmological distance, Nature (London) 481, 341 (2012).
- [49] S. Vegetti, L. V. E. Koopmans, M. W. Auger, T. Treu, and A. S. Bolton, Inference of the cold dark matter substructure mass function at z = 0.2 using strong gravitational lenses, Mon. Not. R. Astron. Soc. **442**, 2017 (2014).
- [50] S. Birrer, A. Amara, and A. Refregier, Lensing substructure quantification in RXJ1131-1231: A 2 keV lower bound on dark matter thermal relic mass, J. Cosmol. Astropart. Phys. 05 (2017) 037.
- [51] S. Vegetti, G. Despali, M. R. Lovell, and W. Enzi, Constraining sterile neutrino cosmologies with strong gravitational lensing observations at redshift $z \sim 0.2$, Mon. Not. R. Astron. Soc. **481**, 3661 (2018).
- [52] D. Gilman, S. Birrer, T. Treu, A. Nierenberg, and A. Benson, Probing dark matter structure down to 10⁷ solar masses: Flux ratio statistics in gravitational lenses with line-of-sight haloes, Mon. Not. R. Astron. Soc. 487, 5721 (2019).
- [53] J.-W. Hsueh, W. Enzi, S. Vegetti, M. W. Auger, C. D. Fassnacht, G. Despali, L. V. E. Koopmans, and J. P. McKean, SHARP—VII. New constraints on the dark matter free-streaming properties and substructure abundance from gravitationally lensed quasars, Mon. Not. R. Astron. Soc. 492, 3047 (2019).
- [54] D. Gilman, S. Birrer, A. Nierenberg, T. Treu, X. Du, and A. Benson, Warm dark matter chills out: Constraints on the halo mass function and the free-streaming length of dark matter with eight quadruple-image strong gravitational lenses, Mon. Not. R. Astron. Soc. 491, 6077 (2020).
- [55] D. Boyanovsky, Clustering properties of a sterile neutrino dark matter candidate, Phys. Rev. D 78, 103505 (2008).
- [56] D. Boyanovsky and J. Wu, Small scale aspects of warm dark matter: Power spectra and acoustic oscillations, Phys. Rev. D 83, 043524 (2011).
- [57] J.-L. Kuo, M. Lattanzi, K. Cheung, and J. W. F. Valle, Decaying warm dark matter and structure formation, J. Cosmol. Astropart. Phys. 12 (2018) 026.
- [58] N. Menci, A. Grazian, A. Lamastra, F. Calura, M. Castellano, and P. Santini, Galaxy formation in sterile neutrino dark matter models, Astrophys. J. 854, 1 (2018).
- [59] A. Boyarsky, A. Neronov, O. Ruchayskiy, and M. Shaposhnikov, Constraints on sterile neutrinos as a dark matter candidate from the diffuse x-ray background, Mon. Not. R. Astron. Soc. 370, 213 (2006).
- [60] S. Riemer-Sørensen and S. H. Hansen, Decaying dark matter in the Draco dwarf galaxy, Astron. Astrophys. 500, L37 (2009).
- [61] S. Horiuchi, P. J. Humphrey, J. Onorbe, K. N. Abazajian, M. Kaplinghat, and S. Garrison-Kimmel, Sterile neutrino dark matter bounds from galaxies of the Local Group, Phys. Rev. D 89, 025017 (2014).

- [62] C. R. Watson, J. F. Beacom, H. Yuksel, and T. P. Walker, Direct x-ray constraints on sterile neutrino warm dark matter, Phys. Rev. D 74, 033009 (2006).
- [63] D. Malyshev, A. Neronov, and D. Eckert, Constraints on 3.55 keV line emission from stacked observations of dwarf spheroidal galaxies, Phys. Rev. D 90, 103506 (2014).
- [64] D. Iakubovskyi, E. Bulbul, A. R. Foster, D. Savchenko, and V. Sadova, Testing the origin of ~3.55 keV line in individual Galaxy clusters observed with XMM-Newton, arXiv:1508.05186.
- [65] M. Loewenstein, A. Kusenko, and P. L. Biermann, New limits on sterile neutrinos from Suzaku observations of the Ursa Minor dwarf spheroidal galaxy, Astrophys. J. 700, 426 (2009).
- [66] H. Yuksel, J. F. Beacom, and C. R. Watson, Strong upper limits on sterile neutrino warm dark matter, Phys. Rev. Lett. 101, 121301 (2008).
- [67] E. Carlson, T. Jeltema, and S. Profumo, Where do the 3.5 keV photons come from? A morphological study of the Galactic center and of Perseus, J. Cosmol. Astropart. Phys. 02 (2015) 009.
- [68] S. Riemer-Sørensen, Constraints on the presence of a 3.5 keV dark matter emission line from Chandra observations of the Galactic centre, Astron. Astrophys. 590, A71 (2016).
- [69] T. E. Jeltema and S. Profumo, Discovery of a 3.5 keV line in the Galactic centre and a critical look at the origin of the line across astronomical targets, Mon. Not. R. Astron. Soc. 450, 2143 (2015).
- [70] M. E. Anderson, E. Churazov, and J. N. Bregman, Nondetection of x-ray emission from sterile neutrinos in stacked galaxy spectra, Mon. Not. R. Astron. Soc. 452, 3905 (2015).
- [71] O. Urban, N. Werner, S. W. Allen, A. Simionescu, J. S. Kaastra, and L. E. Strigari, A Suzaku search for dark matter emission lines in the x-ray brightest galaxy clusters, Mon. Not. R. Astron. Soc. 451, 2447 (2015).
- [72] N. Sekiya, N. Y. Yamasaki, and K. Mitsuda, A search for a keV signature of radiatively decaying dark matter with Suzaku XIS observations of the x-ray diffuse background, Publ. Astron. Soc. Jpn. 68, S31 (2016).
- [73] E. Figueroa-Feliciano *et al.* (XQC Collaboration), Searching for keV sterile neutrino dark matter with x-ray microcalorimeter sounding rockets, Astrophys. J. **814**, 82 (2015).
- [74] T. E. Jeltema and S. Profumo, Deep XMM observations of Draco rule out at the 99% confidence level a dark matter decay origin for the 3.5 keV line, Mon. Not. R. Astron. Soc. 458, 3592 (2016).
- [75] J. Franse *et al.*, Radial profile of the 3.55 keV line out to R₂₀₀ in the Perseus cluster, Astrophys. J. **829**, 124 (2016).
- [76] E. Bulbul, M. Markevitch, A. Foster, E. Miller, M. Bautz, M. Loewenstein, S. W. Randall, and R. K. Smith, Searching for the 3.5 keV line in the stacked Suzaku observations of galaxy clusters, Astrophys. J. 831, 55 (2016).
- [77] F. Hofmann, J. S. Sanders, K. Nandra, N. Clerc, and M. Gaspari, 7.1 keV sterile neutrino constraints from x-ray observations of 33 clusters of galaxies with Chandra ACIS, Astron. Astrophys. **592**, A112 (2016).

- [78] F. A. Aharonian *et al.* (Hitomi Collaboration), Hitomi constraints on the 3.5 keV line in the Perseus galaxy cluster, Astrophys. J. **837**, L15 (2017).
- [79] N. Cappelluti, E. Bulbul, A. Foster, P. Natarajan, M. C. Urry, M. W. Bautz, F. Civano, E. Miller, and R. K. Smith, Searching for the 3.5 keV line in the deep fields with Chandra: The 10 Ms observations, Astrophys. J. 854, 179 (2018).
- [80] A. Boyarsky, D. Iakubovskyi, O. Ruchayskiy, and D. Savchenko, Surface brightness profile of the 3.5 keV line in the Milky Way Halo, arXiv:1812.10488.
- [81] T. Tamura *et al.*, An x-ray spectroscopic search for dark matter and unidentified line signatures in the Perseus cluster with Hitomi, Publ. Astron. Soc. Jpn. **71** (2019).
- [82] C. Dessert, N. L. Rodd, and B. R. Safdi, The dark matter interpretation of the 3.5-keV line is inconsistent with blank-sky observations, Science 367, 1465 (2020).
- [83] F. Hofmann and C. Wegg, 7.1 keV sterile neutrino dark matter constraints from a deep Chandra x-ray observation of the Galactic bulge limiting window, Astron. Astrophys. 625, L7 (2019).
- [84] K. N. Abazajian, Resonantly Produced 7 keV Sterile Neutrino Dark Matter Models and the Properties of Milky Way Satellites, Phys. Rev. Lett. 112, 161303 (2014).
- [85] D. P. Finkbeiner and N. Weiner, X-ray line from exciting dark matter, Phys. Rev. D 94, 083002 (2016).
- [86] T. Higaki, K. S. Jeong, and F. Takahashi, The 7 keV axion dark matter and the x-ray line signal, Phys. Lett. B 733, 25 (2014).
- [87] V. Brdar, J. Kopp, J. Liu, and X.-P. Wang, X-ray Lines from Dark Matter Annihilation at the KeV Scale, Phys. Rev. Lett. 120, 061301 (2018).
- [88] M. H. Namjoo, T. R. Slatyer, and C.-L. Wu, Enhanced n-body annihilation of dark matter and its indirect signatures, J. High Energy Phys. 03 (2019) 077.
- [89] K. Nakayama, F. Takahashi, and T. T. Yanagida, Revisiting the number-theory dark matter scenario and the weak gravity conjecture, Phys. Lett. B **790**, 218 (2019).
- [90] L. Gu, J. Kaastra, A. J. J. Raassen, P. D. Mullen, R. S. Cumbee, D. Lyons, and P. C. Stancil, A novel scenario for the possible x-ray line feature at ~3.5 keV: Charge exchange with bare sulfur ions, Astron. Astrophys. **584**, L11 (2015).
- [91] L. Gu, J. Mao, J. de Plaa, A. J. J. Raassen, C. Shah, and J. S. Kaastra, Charge exchange in galaxy clusters, Astron. Astrophys. 611, A26 (2018).
- [92] E. G. Speckhard, K. C. Y. Ng, J. F. Beacom, and R. Laha, Dark Matter Velocity Spectroscopy, Phys. Rev. Lett. 116, 031301 (2016).
- [93] D. Powell, R. Laha, K. C. Y. Ng, and T. Abel, Doppler effect on indirect detection of dark matter using dark matter only simulations, Phys. Rev. D 95, 063012 (2017).
- [94] F. A. Harrison *et al.*, The Nuclear Spectroscopic Telescope Array (NuSTAR) high-energy x-ray mission, Astrophys. J. 770, 103 (2013).
- [95] D. R. Wik *et al.*, NuSTAR observations of the Bullet Cluster: Constraints on inverse Compton emission, Astrophys. J. **792**, 48 (2014).

- [96] K. K. Madsen *et al.*, Calibration of the NuSTAR high energy focusing x-ray telescope, Astrophys. J. Suppl. Ser. 220, 8 (2015).
- [97] R. A. Krivonos, S. S. Tsygankov, I. A. Mereminskiy, A. A. Lutovinov, S. Yu. Sazonov, and R. A. Sunyaev, New hard x-ray sources discovered in the ongoing INTEGRAL Galactic plane survey after 14 years of observations, Mon. Not. R. Astron. Soc. 470, 512 (2017).
- [98] R. Launhardt, R. Zylka, and P. G. Mezger, The nuclear bulge of the galaxy. III. Large scale physical characteristics of stars and interstellar matter, Astron. Astrophys. 384, 112 (2002).
- [99] M. Revnivtsev, S. Molkov, and S. Sazonov, Map of the Galaxy in the 6.7-keV emission line, Mon. Not. R. Astron. Soc. Lett. 373, L11 (2006).
- [100] T. Prusti et al., The Gaia mission, Astron. Astrophys. 595, A1 (2016).
- [101] A. G. A. Brown *et al.* (Gaia Collaboration), Gaia Data Release 2. Summary of the contents and survey properties, Astron. Astrophys. 616, A1 (2018).
- [102] W. Voges et al., The ROSAT all-sky survey bright source catalogue, Astron. Astrophys. 349, 389 (1999).
- [103] H. Mori, Y. Maeda, Y. Ueda, T. Dotani, and M. Ishida, Suzaku observations of unidentified x-ray sources toward the Galactic bulge, Publ. Astron. Soc. Jpn. 64 (2012).
- [104] H. An, K. K. Madsen, N. J. Westergaard, S. E. Boggs, F. E. Christensen, W. W. Craig, C. J. Hailey, F. A. Harrison, D. K. Stern, and W. W. Zhang, In-flight PSF calibration of the NuSTAR hard x-ray optics, Proc. SPIE Int. Soc. Opt. Eng. 9144, 91441Q (2014).
- [105] D. E. Gruber, J. L. Matteson, L. E. Peterson, and G. V. Jung, The spectrum of diffuse cosmic hard x-rays measured with HEAO-1, Astrophys. J. 520, 124 (1999).
- [106] E. Churazov *et al.*, INTEGRAL observations of the cosmic x-ray background in the 5–100 keV range via occultation by the earth, Astron. Astrophys. **467**, 529 (2006).
- [107] H. Kaneda, K. Makishima, S. Yamauchi, K. Koyama, K. Matsuzaki, and N. Y. Yamasaki, Complex spectra of the Galactic ridge x-rays observed with ASCA, Astrophys. J. 491, 638 (1997).
- [108] T. Yuasa, K. Makishima, and K. Nakazawa, Broadband spectral analysis of the Galactic ridge x-ray emission, Astrophys. J. 753, 129 (2012).
- [109] K. Perez, R. Krivonos, and D. R. Wik, The Galactic bulge diffuse emission in broad-band x-rays with NuSTAR, Astrophys. J. **884**, 153 (2019).
- [110] R. K. Smith, N. S. Brickhouse, D. A. Liedahl, and J. C. Raymond, Collisional plasma models with APEC/APED: Emission-line diagnostics of hydrogen-like and heliumlike ions, Astrophys. J. **556**, L91 (2001).
- [111] S. Sazonov, E. Churazov, R. Sunyaev, and M. Revnivtsev, Hard x-ray emission of the Earth's atmosphere: Monte Carlo simulations, Mon. Not. R. Astron. Soc. 377, 1726 (2007).
- [112] E. Churazov, S. Sazonov, R. Sunyaev, and M. Revnivtsev, Earth x-ray Albedo for cosmic x-ray background radiation in the 1–1000 keV band, Mon. Not. R. Astron. Soc. **385**, 719 (2008).

- [113] V. Fioretti, A. Bulgarelli, G. Malaguti, V. Bianchin, M. Trifoglio, and F. Gianotti, The low earth orbit radiation environment and its impact on the prompt background of hard x-ray focusing telescopes, in *High Energy, Optical, and Infrared Detectors for Astronomy V*, edited by Andrew D. Holland and James W. Beletic, International Society for Optics and Photonics Vol. 8453 (SPIE, Bellingham, WA, 2012). p. 833.
- [114] F. A. Harrison *et al.* (NuSTAR Collaboration), The NuSTAR extragalactic surveys: The number counts of active galactic nuclei and the resolved fraction of the cosmic x-ray background, Astrophys. J. **831**, 185 (2016).
- [115] M. Revnivtsev, S. Sazonov, E. Churazov, W. Forman, A. Vikhlinin, and R. Sunyaev, Discrete sources as the origin of the Galactic x-ray ridge emission, Nature (London) 458, 1142 (2009).
- [116] R. Krivonos, S. Tsygankov, M. Revnivtsev, S. Sazonov, E. Churazov, and R Sunyaev, INTEGRAL constraints on the Galactic hard x-ray background from the Milky Way anticenter, Astron. Astrophys. **537**, A92 (2012).
- [117] M. G. Revnivtsev and S. V. Molkov, Results from a deep RXTE/PCA scan across the Galactic plane, Mon. Not. R. Astron. Soc. 424, 2330 (2012).
- [118] J. Wilms, A. Allen, and R. McCray, On the absorption of x-rays in the interstellar medium, Astrophys. J. 542, 914 (2000).
- [119] J. M. Dickey and F. J. Lockman, HI in the Galaxy, Annu. Rev. Astron. Astrophys. **28**, 215 (1990).
- [120] P. M. W. Kalberla, W. B. Burton, D. Hartmann, E. M. Arnal, E. Bajaja, R. Morras, and W. G. L. Pöppel, The Leiden/Argentine/Bonn (LAB) survey of Galactic HI: Final data release of the combined LDS and IAR surveys with improved stray-radiation corrections, Astron. Astrophys. 440, 775 (2005).
- [121] J. F. Navarro, C. S. Frenk, and S. D. M. White, A universal density profile from hierarchical clustering, Astrophys. J. 490, 493 (1997).
- [122] D. Hooper, The density of dark matter in the Galactic bulge and implications for indirect detection, Phys. Dark Universe **15**, 53 (2017).
- [123] M. Pato, F. Iocco, and G. Bertone, Dynamical constraints on the dark matter distribution in the Milky Way, J. Cosmol. Astropart. Phys. 12 (2015) 001.
- [124] A. Boehle *et al.*, An improved distance and mass estimate for Sgr A* from a multistar orbit analysis, Astrophys. J. **830**, 17 (2016).
- [125] R. Abuter *et al.* (GRAVITY Collaboration), A geometric distance measurement to the Galactic center black hole with 0.3% uncertainty, Astron. Astrophys. **625**, L10 (2019).
- [126] F. Nesti and P. Salucci, The dark matter halo of the Milky Way, AD 2013, J. Cosmol. Astropart. Phys. 07 (2013) 016.
- [127] F. Calore, N. Bozorgnia, M. Lovell, G. Bertone, M. Schaller, C. S. Frenk, R. A. Crain, J. Schaye, T. Theuns, and J. W. Trayford, Simulated Milky Way analogues: Implications for dark matter indirect searches, J. Cosmol. Astropart. Phys. 12 (2015) 053.
- [128] M. Schaller *et al.*, Dark matter annihilation radiation in hydrodynamic simulations of Milky Way haloes, Mon. Not. R. Astron. Soc. **455**, 4442 (2016).

- [129] A. Burkert, The structure of dark matter halos in dwarf galaxies, Astrophys. J. Lett. **447**, L25 (1995).
- [130] H.-N. Lin and X. Li, The dark matter profiles in the Milky Way, Mon. Not. R. Astron. Soc. 487, 5679 (2019).
- [131] E. Jones, T. Oliphant, P. Peterson *et al.*, SCIPY: Open source scientific tools for PYTHON, https://www.scipy.org/.
- [132] T. P. Robitaille *et al.* (ASTROPY Collaboration), ASTROPY: A community PYTHON package for astronomy, Astron. Astrophys. **558**, A33 (2013).
- [133] A. M. Price-Whelan *et al.* (ASTROPY Collaboration), The ASTROPY project: Building an open-science project and status of the V2.0 core package, Astron. J. **156**, 123 (2018).